

# On the Competitive Substitutional Partitioning During Nano-pearlitic Transformation in Multicomponent Steels



SNEHASHISH TRIPATHY, P.S. MANORANJAN JENA, VIKASH KUMAR SAHU, SUDIP KUMAR SARKAR, SARITA AHLAWAT, ANIRUDDHA BISWAS, BHUPESHWAR MAHATO, SOUMITRO TARAFDER, and SANDIP GHOSH CHOWDHURY

Bulk nano-pearlitic microstructure with apparent interlamellar spacing below 100 nm has been attained by rapidly undercooling a hypereutectoid multicomponent steel below equilibrium eutectoid temperature from the austenitization temperature. The aforementioned processing rendered non-partitioned pearlite growth in the steel, as confirmed by acquiring compositional variation across the austenite/pearlite growth front using scanning transmission electron microscopy coupled with energy dispersive X-ray spectroscopy (STEM-EDS) technique. The post transformation sidewise partitioning of substitutional components between ferrite and cementite has been critically assessed by interrupting the cooling process at various intervals followed by STEM-EDS and atom probe tomography (APT) across the austenite/pearlite and ferrite/cementite interfaces. This partitioning phenomena has been simulated using DICTRA<sup>®</sup> and validated with experimental observations. It is inferred that partitioning kinetics of Mn is fastest in the early stages followed by Cr in the intermediate. However, towards the completion stages of partitioning, Mn and Si have much faster rate as compared to Cr.

<https://doi.org/10.1007/s11661-022-06635-z>

© The Minerals, Metals & Materials Society and ASM International 2022

## I. INTRODUCTION

PEARLITE formation in ternary steels has been investigated extensively with an attempt to understand the transformation course by means of different local equilibrium (LE) based models (viz. either ‘para-’ or ‘quasi para-’ or ‘ortho-’). With the help of these LE models, theoretical evaluation of growth rate, interlamellar spacing, volume fraction of phases etc. are done and often validated with experimental observations.<sup>[1–11]</sup> These seminal LE models have been elaborately laid out by various researchers.<sup>[7,12–15]</sup> One of the key takeaways from the hitherto developed understanding is that

pearlite may form without long range substitutional partitioning, under what are commonly termed as para-equilibrium (PE) or no-partitioning local equilibrium (NPLE) conditions.<sup>[5,7,10]</sup> However, quantitative evidences of such prevalent LE conditions through compositional analysis across advancing pearlite/austenite ( $\gamma$ ) interface are merely few.<sup>[16–24]</sup> Among these, only the studies carried out by Hutchinson *et al.*<sup>[22]</sup> and Aranda *et al.*<sup>[23,24]</sup> have adopted the usage of advanced analytical transmission electron microscopy (ATEM) for assessing LE conditions in partitioned pearlite. This scarcity of direct experimental evidence is even more prominent for non-partitioned pearlite growth, as most of the studies which could have potentially identified such transformation condition simply lacked the required level of resolution for compositional analysis.<sup>[16–21]</sup> In the studies carried out on ternary steels containing Cr, Mn, Si, Ni etc. by Ridley *et al.*, a no-partitioning temperature could not be clearly identified based upon the compositional analysis across the growth front of pearlite.<sup>[16–21]</sup> This can be attributed to the limited spatial resolution of the adopted techniques leading to unavoidable contribution from regions experiencing post transformation effects, which was realized by Ridley *et al.* while re-examining the partitioning behaviour of Cr and Mn.<sup>[17,19]</sup> Recently,

SNEHASHISH TRIPATHY, P.S. MANORANJAN JENA, VIKASH KUMAR SAHU, SOUMITRO TARAFDER, and SANDIP GHOSH CHOWDHURY are with the Academy of Scientific and Innovative Research (AcSIR), Ghaziabad 201002, India and also with the CSIR - National Metallurgical Laboratory, Jamshedpur 831007, India. Contact e-mail: [sgc@nmlindia.org](mailto:sgc@nmlindia.org) SUDIP KUMAR SARKAR, SARITA AHLAWAT, and ANIRUDDHA BISWAS are with the Glass and Advanced Materials Division, Bhabha Atomic Research Center, Mumbai, 400085, India.. BHUPESHWAR MAHATO is with the CSIR - National Metallurgical Laboratory.

Manuscript submitted September 28, 2021; accepted February 12, 2022.  
Article published online March 7, 2022

in yet another intriguing attempt for understanding the pearlite transformation mechanism under NPLE mode in Fe-C-Mn alloys, Ishigami *et al.* adopted scanning transmission electron microscopy coupled with energy dispersive X-ray spectroscopy (STEM-EDS) technique.<sup>[25]</sup> Here, STEM-EDS technique was employed to characterize the compositional variation across the pearlite/austenite interface. The observation of compositional spike (of Mn) at the ferrite/austenite interface for pearlite growing under NPLE condition has been presented by the authors. However, the acquisition conditions maintained during STEM-EDS linescan along with the appropriate compositional corrections adopted by the authors have not been elaborately laid down, because of which the reliability of the presented data cannot be asserted. Therefore, it can unambiguously be stated that non-partitioned pearlite formation, which is an expected phenomena in most of the continuously cooled steel products has not been observationally studied yet for multicomponent steels.

This scenario coupled with the quest for development of nano-structured advanced high strength steels,<sup>[26–28]</sup> motivated the present research work. Nano-pearlitic steels are industrially processed by rapid undercooling below the equilibrium transformation temperature ( $T_{\text{Eutectoid}}$ ), followed by non-isothermal cooling till room temperature.<sup>[27,28]</sup> Under such conditions, there may exist possibilities of non-partitioned pearlite growth, for which as already mentioned, no experimental investigation have been carried out so far unlike ferrite.<sup>[15,29–33]</sup> Consequently, the information about post transformation partitioning (towards full equilibrium condition) also remains unknown. The studies by Ridley *et al.* on various Fe-M-C ternaries (M = Mn, Cr, Si etc.) and a few Fe-M-N-C quaternaries (M,N = Mn, Cr, Ni) provide some assessment of the post transformation partitioning kinetics.<sup>[17–19,21]</sup> Amongst Mn and Cr, it has been observed by Ridley *et al.* that rate of post transformation partitioning for Cr is always greater than that of Mn.<sup>[17]</sup> The faster rate of partitioning of Cr, despite of possessing lower diffusivity in ferrite as compared to Mn, has been related to the greater affinity of the former towards cementite. However it has also been reported by Ridley *et al.* that unlike Si, the post transformation partitioning of Mn and Cr from ferrite to cementite is not significantly discernible at short distances from the growth front (*i.e.*, at smaller post transformation time intervals). This has been attributed to the rapid diffusion of Si from cementite to ferrite owing to negligible solubility of Si in cementite.<sup>[17,18]</sup> The post transformation partitioning results of the aforementioned ternaries or quaternaries have not been treated after deconvoluting the contribution from partitioning during transformation, thereby leading only to a qualitative viewpoint on the partitioning rate. Moreover, none of the post transformation studies are carried out on ternaries or quaternaries forming non-partitioned pearlite, which is why, cannot be extended directly to multicomponent steels such as the ones produced industrially. This unexplored fundamental information possesses key technological relevance as it would yield an understanding about post

transformation compositional evolution within the ferrite/cementite lamellae. There also lie possibilities of ferrite ( $\alpha$ )/cementite ( $\theta$ ) interfacial enrichment owing to the differential diffusivities of substitutional elements in both phases. A precise knowledge about the temporal variation of substitutional content within  $\alpha/\theta$  lamellae would help in designing pearlitic steels with additional contribution from solid solution strengthening. Even the reminiscent interfacial segregations arising due to drastic differences in diffusivities of components in different phases have recently been shown to render additional strengthening and stability in engineered materials.<sup>[34–38]</sup>

In light of the absence of thorough experimental assessment of post transformation partitioning kinetics in pearlitic steels, the present study has been undertaken. In this work, therefore, an attempt has been made to experimentally evaluate the partitioning kinetics of substitutional elements post nano-pearlitic transformation, where majority of the pearlite growth happened under no-partitioning condition. This evaluation has been carried out by employing high resolution spectroscopic characterization across pearlite/austenite and ferrite/cementite interfaces in samples interrupted at different instances of pearlite formation. Further the observed competitive partitioning rates of different components are correlated with the respective diffusivities and stabilizing effects (chemical potential) in different phases.

## II. EXPERIMENTAL PROCEDURE

In line with the aforementioned target to assess the partitioning behaviour of different substitutional components post pearlitic transformation, a multicomponent hypereutectoid steel was designed. The designed alloy was processed targeting nano-pearlitic microstructure with apparent interlamellar spacing below 100 nm. The steel (composition in Table I) was prepared by induction melting and ingot casting route. The cast ingot was homogenized at 1250 °C for 180 minutes followed by hot forging into slab of 30mm thickness. The forged slab was subsequently furnace cooled from 1250 °C till room temperature (RT). Sample of dimension 100 mm × 50 mm × 30 mm prepared out of the forged slab was soaked at 1050 °C for 75 minutes followed by hot rolling (to a thickness of 15 mm) and recrystallization annealing at 1050 °C for 60 minutes. Subsequently, samples of dimension 20 mm × 15 mm × 10 mm were extracted from the annealed slabs avoiding the decarburized layer. In order to ensure a fully pearlitic microstructure with interlamellar spacing < 100 nm, the samples were re-austenitized at 990 °C followed by forced air cooling through the  $A_{\text{CM}}$  to  $T_{\text{U}}$  (undercooling temperature below  $T_{\text{Eutectoid}}$  *i.e.*, ~ 750 °C as obtained from ThermoCalc<sup>®</sup> with TCFE9 database) temperature regime. This undercooling temperature was set as 680 °C so that the designed composition could lie inside the Hultgren's extrapolation area wherein mutual supersaturation of  $\gamma$  with respect to both  $\alpha$  and  $\theta$  can be attained.<sup>[5,9]</sup> The Hultgren's extrapolation area is highlighted by the hatched region in Figure 1(a) wherein the

**Table I. Composition of the Designed Alloy**

Elements	C	Mn	Si	Cr	P	S	Fe
Content in wt pct	1.0	0.9	1.1	0.9	< 0.03	< 0.006	Bal.

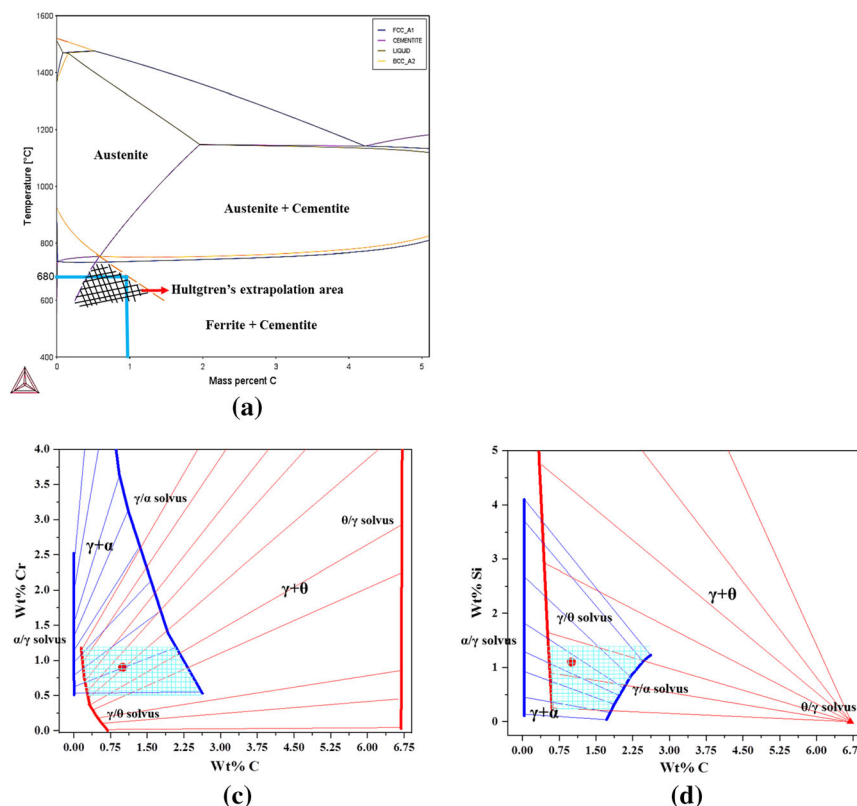


Fig. 1—(a) Temperature vs. Carbon content phase diagram for a Fe-0.9Mn-1.1Si-0.9Cr system, computed using ThermoCalc<sup>®</sup> with TCFE9 database. Hatched region shows the Hultgren's extrapolated area surrounded by the extrapolated  $\alpha/\gamma$  and  $\theta/\gamma$  solvus curves Metastable  $\alpha/\gamma$ ,  $\gamma/\alpha$ ,  $\theta/\gamma$  and  $\gamma/\theta$  solvus curves along with corresponding equilibrium tie lines computed by Unified Interaction Parameter Formalism, at 680 °C for: (b) Fe-Mn-C; (c) Fe-Cr-C and (d) Fe-Si-C ternaries, here the red dots represent the nominal alloy composition positioned in each ternary diagram; and the hatched region represents the Hultgren's extrapolated area (Color figure online).

phase diagram for the designed composition simulated using ThermoCalc<sup>®</sup> with TCFE9 database has been shown. The undercooling temperature of 680 °C for the designed alloy (carbon content) has been shown to lie inside the Hultgren's extrapolation area in Figure 1(a), thereby confirming the tendency of complete pearlitic transformation. Further with the thermodynamic consideration that interactions amongst various components usually do not extend significantly beyond ternaries, the designed composition was split into pseudo ternaries of Fe-M-C (where, M = Mn, Si and Cr) for metastable isothermal phase diagram evaluation. The metastable  $\gamma/\alpha$  and  $\gamma/\theta$  phase boundaries at 680 °C were determined by adopting Unified Interaction Parameter Formalism<sup>[39–42]</sup> and shown for each ternary in Figures 1(b) through (d). The interaction parameters were determined using various equilibrium composition values for  $\alpha/\gamma$ ,  $\gamma/\alpha$ ,  $\theta/\gamma$  and  $\gamma/\theta$  (obtained from stable isothermal phase diagrams generated by ThermoCalc<sup>®</sup> with TCFE9 database), in the expressions for

activity coefficients.<sup>[39–42]</sup> The phase diagrams obtained by Unified Interaction Parameter Formalism did conform to the predicted phase diagrams of ThermoCalc<sup>®</sup> (although this validation has not been included here). The treatment in terms of pseudo-ternaries was done so as to individually assess the satisfaction of mutual supersaturation criterion for each substitutional component. Since pearlitic transformation is known to be associated with the possibility of negligible substitutional partitioning, the assessment in terms of pseudo-ternaries clarifies the preliminary stance of individual element with respect to simultaneous formation of ferrite and cementite by diffusion. From the calculated metastable isothermal phase diagrams for various pseudo ternaries at 680 °C, it was ensured that the mutual supersaturation exists for all the alloying elements.

Once the specimen attained  $T_U$ , the second stage of slow cooling commenced inside a pre-heated refractory brick, targeting fully pearlitic microstructure. In order

to monitor the exact cooling rates experienced by the samples in the different stages, K-type thermocouples were spot welded at the center and data was acquired during the entire heat treatment schedule. Samples were interrupted during the second stage cooling at different time instances by quenching in water. The interrupted specimens were studied for growth rate measurements using FEI Nova Nano 430 field emission scanning electron microscope (FE-SEM). Furthermore, three samples were interrupted by quenching in water after a lapse of ~ 30, 70 and 150 seconds in the 2<sup>nd</sup> stage corresponding to approximate temperatures of 670 °C, 660 °C and 635 °C (designated as S1, S2 and S3 respectively). These interruptions were intended to characterize the partitioning across the advancing pearlite/austenite interface during transformation as well as post transformation partitioning across ferrite/cementite interface by transmission electron microscopy.

The partitioning studies were carried out on S1, S2 and S3 specimens using STEM - EDS technique in a JEOL JEM 2200FS TEM equipped with an Oxford windowless EDS detector of 80mm<sup>2</sup> opening. Thin foil samples were prepared by electropolishing in a 90 pct acetic acid + 10 pct perchloric acid solution at ~15 °C, maintaining current in the range of 35-40 mA. After electropolishing, the thin foil was subjected to ion milling in a Gatan Pips II ion miller system at a shallow angle of 3° and voltage of 0.5 kV to get rid of surface oxide and to attain uniformity in surface relief. Before X-ray acquisition, it was ensured in each case that strong two beam conditions are not prevalent so as to avoid any channeling effect. The exact position and alignment of the austenite/pearlite interface was based upon that of the  $\gamma/\theta$  interphase boundary as it was observed to possess much sharper contrast as compared to the  $\gamma/\alpha$  boundary, when maintained parallel to the electron beam. The X-ray acquisition was carried out along linear equidistant multi-point arrays programmed using INCA Oxford EDS software. These linear arrays were positioned across  $\gamma/\theta$ ,  $\gamma/\alpha$  and  $\alpha/\theta/\alpha$  interfaces with different spacing between the points in each case. In case of S3 barely any residual austenite could be observed, due to which multi-point EDS were acquired only across  $\alpha/\theta/\alpha$  interface. The distance between each point during the STEM EDS scan and the consequent number of points in the linear array was decided keeping in view the trade-off between sufficient exposure time for X-ray acquisition and inevitable drift rates at high magnification. A probe size of 0.7 nm was used with live acquisition time of 35 seconds at each point. This acquisition time was sufficient for collection of several thousand counts of X-rays for each element owing to the high probe current (*i.e.*, ~0.5nA at 1 nm spot size) achieved in the Analytical MAG (A-MAG) mode in STEM. In addition, a large condenser aperture (of 100 $\mu$ m covering the azimuth of Ronchigram) also enhanced EDS counts. The stray X-ray induced background was minimized by inserting hard X-ray aperture. A thin foil specimen in the solution annealed and quenched condition of the same alloy, prepared by the aforementioned procedure was used for determining the Cliff-Lorimer ( $k_{j/Fe}$ ) factors for different alloying

elements.<sup>[17,18,43]</sup> The range of thicknesses assessed during  $k_{j/Fe}$  determination step, indicated at the possible fluorescence of Cr K $\alpha$  by Fe K $\alpha$ , the correction for which was additionally incorporated into the  $k_{Cr/Fe}$  factor. The contribution of Cr K $\beta$  to Mn K $\alpha$  was also subtracted as per procedures adopted by Ridley *et al.*<sup>[17,19]</sup> Background subtracted integrated X-ray intensities were converted into concentration of substitutional elements adopting standard Cliff-Lorimer approach and the determined  $k_{j/Fe}$  factors.<sup>[16-18,22,43]</sup>

Further assessment of this competitive post transformation substitutional partitioning and reminiscent interfacial enrichment (if any) was carried out by Atom Probe Tomography (APT) for a specimen quenched after a lapse of 1100 seconds in the 2<sup>nd</sup> stage cooling (*i.e.*, ~350 °C) and designated as S4. APT specimen was machined to a dimension of 0.3 mm x 0.3 mm x 8 mm followed by electropolishing in two stages using 10 pct perchloric acid + 90 pct methanol and 2 pct perchloric acid + 98 pct butoxyethanol, respectively. APT was carried out with UV laser energy of ~30 nJ under ultrahigh vacuum ~1.5E-10 mbar, using a CAMECA<sup>®</sup> FlexTAP instrument followed by data analysis using IVAS 3.8 software. The specimen temperature was maintained at 30  $\pm$  0.3 K. The data were reconstructed using a voltage-based protocol with the evaporation field of 33 V/nm and detector efficiency of 62 pct. The k-factor and the image compression factor (ICF) were 6.7 and 1.6, respectively. Carbon is known to field evaporate both as mono-atomic and molecular ions and indexing of carbon peaks in the mass spectrum was done accordingly.<sup>[44]</sup> Peaks at the following mass to charge state ratios (m/n): 6, 6.5, 12, 13 Da were indexed as mono-atomic carbon ions, whereas the peaks at 18 and 18.5 Da were assigned to tri-atomic carbon ions.<sup>[44,45]</sup> Composition profiles about the interface were determined using proximity histogram technique, the detailed procedure of which can be found elsewhere.<sup>[46-48]</sup>

### III. RESULTS AND DISCUSSION

#### A. Microstructural Characterization and Growth Rate Measurements

The different cooling rates in the 1<sup>st</sup> and 2<sup>nd</sup> stage were measured to be ~ 5 °C/s and 0.3 °C/s (assuming linear profile), respectively, by the K type thermocouple welded at the center of the samples. The cooling profile as acquired by the thermocouple has been given in Figure 2(a) along with the interruptions carried out for studying the substitutional partitioning behaviour (S1, S2 and S3).

The growth rate of pearlite was measured by adopting the maximum nodule radius (MNR) technique as well as the Cahn and Hagel (CH) method (Figure 2(b)) on the interrupted samples as mentioned in Section II.<sup>[22,49]</sup> In each of these interrupted samples, at least 100 nodules were assessed for determination of MNR. The rate of change of MNR is considered as the steady-state growth rate of pearlite nodule which had nucleated at the early stages of transformation. For growth rate determination

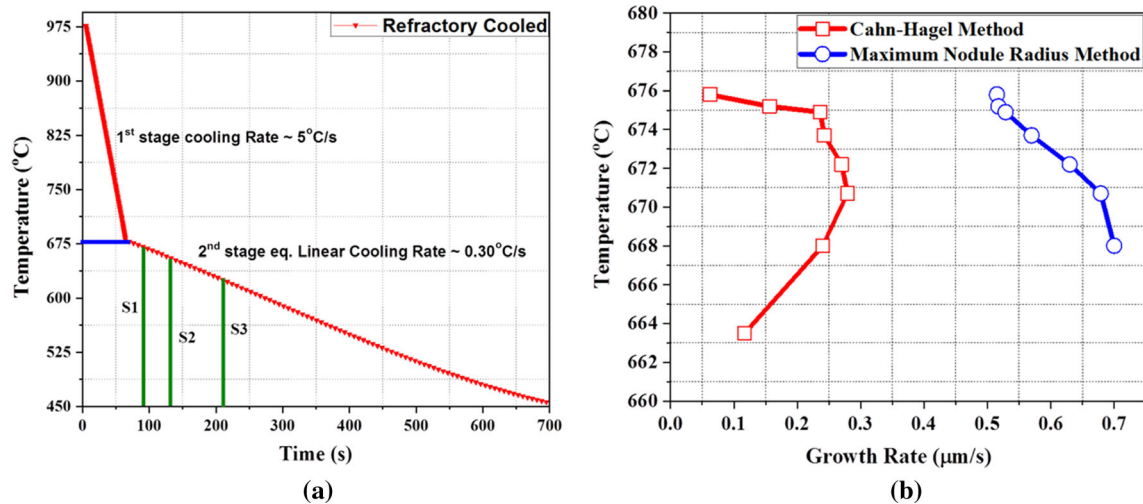


Fig. 2—(a) Post austenitization two stage cooling profile as acquired from the thermocouple welded at the centre of the sample; (b) experimentally measured growth rates by MNR and CH methods.

by CH method, at least 50 micrographs in each sample were assessed. In each micrograph systematic point count technique was adopted to evaluate volume fraction transformed and austenite/pearlite free interface area per unit volume.<sup>[22,49]</sup> The rate of change of volume fraction transformed when averaged over the free austenite/pearlite interfacial area gives the average growth rate of pearlite.<sup>[49]</sup> It was realized that as the transformation nears completion, the MNR technique becomes less reliable (therefore not evaluated beyond ~668 °C) due to the impingement of adjacent nodules.<sup>[22,49]</sup>

The growth rates were observed to increase from ~50 nm/s at ~675 °C to ~300 nm/s at ~670 °C as per the CH method, whereas from ~500 nm/s at ~675 °C to ~700 nm/s at ~670 °C as per the MNR technique.

The reason behind the observed difference is the microstructurally average character of CH method as compared to the spatially subjective character of MNR technique which only considers the fastest growing pearlite nodule.<sup>[22,49]</sup> The assessment using CH method indicates that the growth rate decreases as the transformation nears completion.

## B. Elemental Partitioning Characterization

### 1. Partitioning studies in samples interrupted at 670 °C (S1)

Figure 3(a) and (b) show the STEM bright field (BF) micrograph of a growing pearlite nodule in the S1 specimen wherein the growth direction has been marked. Lines L<sub>1</sub>, L<sub>2</sub> and L<sub>3</sub> shown in Figure 3(b) represent the multi-point linear arrays across  $\theta/\gamma$ ,  $\alpha/\gamma$ ,  $\alpha/\theta/\alpha$  interfaces, respectively, along which EDS was acquired. L<sub>1</sub>, L<sub>2</sub> and L<sub>3</sub> consist of 43, 38 and 34 points with 6, 8 and 1.5 nm separation between the points, respectively. As can be clearly seen from the concentration profiles along L<sub>1</sub>, L<sub>2</sub> in Figures 3(c) and (d), the local composition across the highlighted interface is almost same depicting no partitioning of Si, Mn and Cr

via/at the growth front. The observed partitioning at distances far behind the growth front and the decreasing trend for that towards the interface confirms sidewise post transformation partitioning in case of both L<sub>1</sub> and L<sub>2</sub>. The points farthest from the growth front have experienced maximum duration of post transformation partitioning and hence greater extent of enrichment or depletion as compared to points closer to the interface. The composition profile shown in Figure 3(e) is acquired along L<sub>3</sub> which is positioned ~175 nm from the growth front. From this concentration profile, it can be deduced that the rate of post transformation partitioning of Mn into cementite from ferrite is faster than that of Cr in the S1 specimen.

The minor deviations from smooth profile at some localized regions (*e.g.*, at ~50 nm along L1 for the profile of Si, at ~135 nm along L2 for the profile of Mn etc.) can be attributed to local heterogeneity in sample thickness or any other statistical deviation pertaining to acquired X-ray counts.

### 2. Partitioning studies in samples interrupted at 660 °C (S2)

The STEM BF micrographs of Figures 4(a) and (b) depict a pearlite nodule emanating from a prior austenite grain boundary (highlighted in yellow) in the S2 specimen. Despite the rigorous attempts to tilt the  $\gamma/\theta$  as well as  $\alpha/\theta/\alpha$  interfaces parallel to the electron beam, it could not be attained simultaneously in S2 and is evident from Figure 4(b). Consequently, the observed width of cementite lamellae and hence the interlamellar spacing (Figures 4(a) and (b)) do not represent the true values, rather are merely the projected dimensions. This can also be easily evaluated from Figure 4(b) and (e). The average interlamellar spacing observed in 4(b) is ~137 nm. The thickness of ferrite lamella covered within one interlamellar spacing measurement is ~79 nm. The thickness of cementite lamella covered within one interlamellar spacing measurement is ~58 nm. The ratio of ferrite thickness to cementite thickness is ~1.36

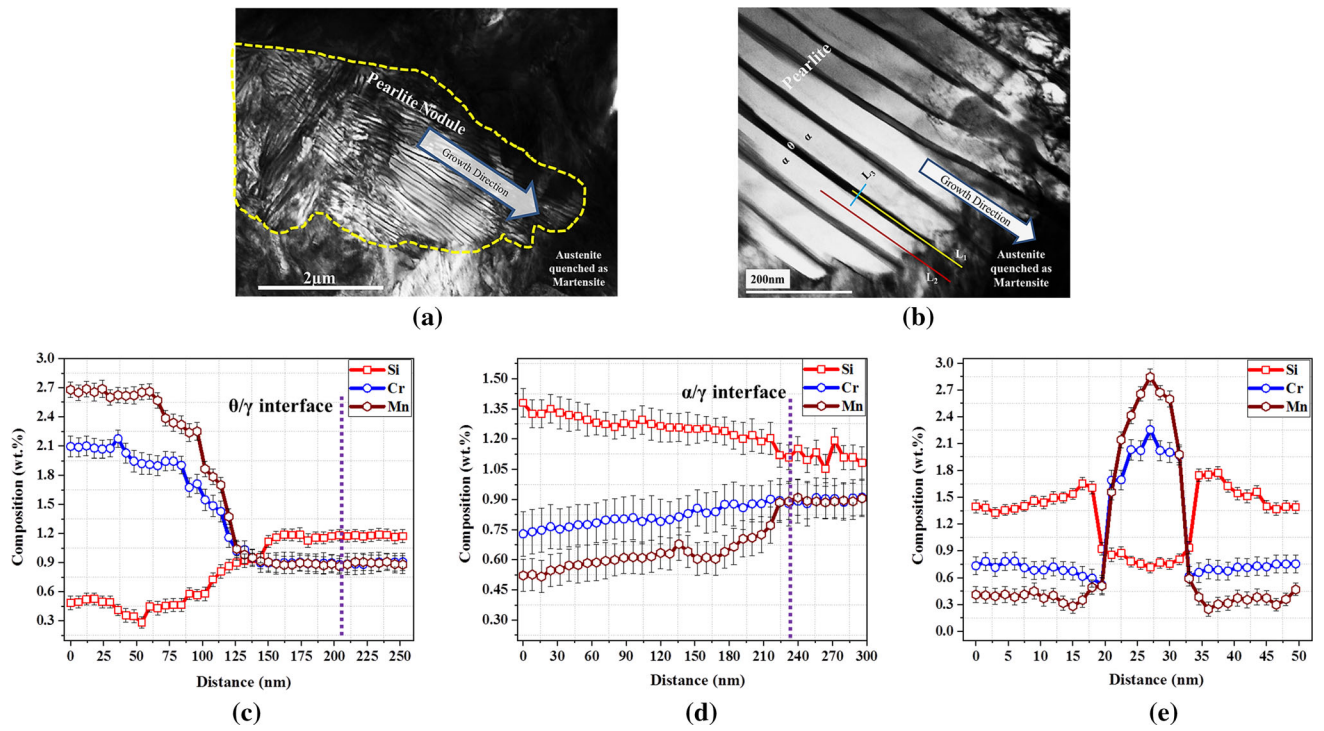


Fig. 3—A growing pearlite nodule in the S1 specimen for which (a) low magnification STEM BF image with the highlighted growth direction and outlined nodule boundary, (b) high-magnification STEM BF image depicting the austenite/pearlite interface and the acquired multi-point EDS arrays along  $L_1$ ,  $L_2$  and  $L_3$ ; composition profile along (c)  $L_1$  across  $\theta/\gamma$  interface, (d)  $L_2$  across  $\alpha/\gamma$  interface and (e)  $L_3$  across  $\alpha/\theta/\alpha$  interface.

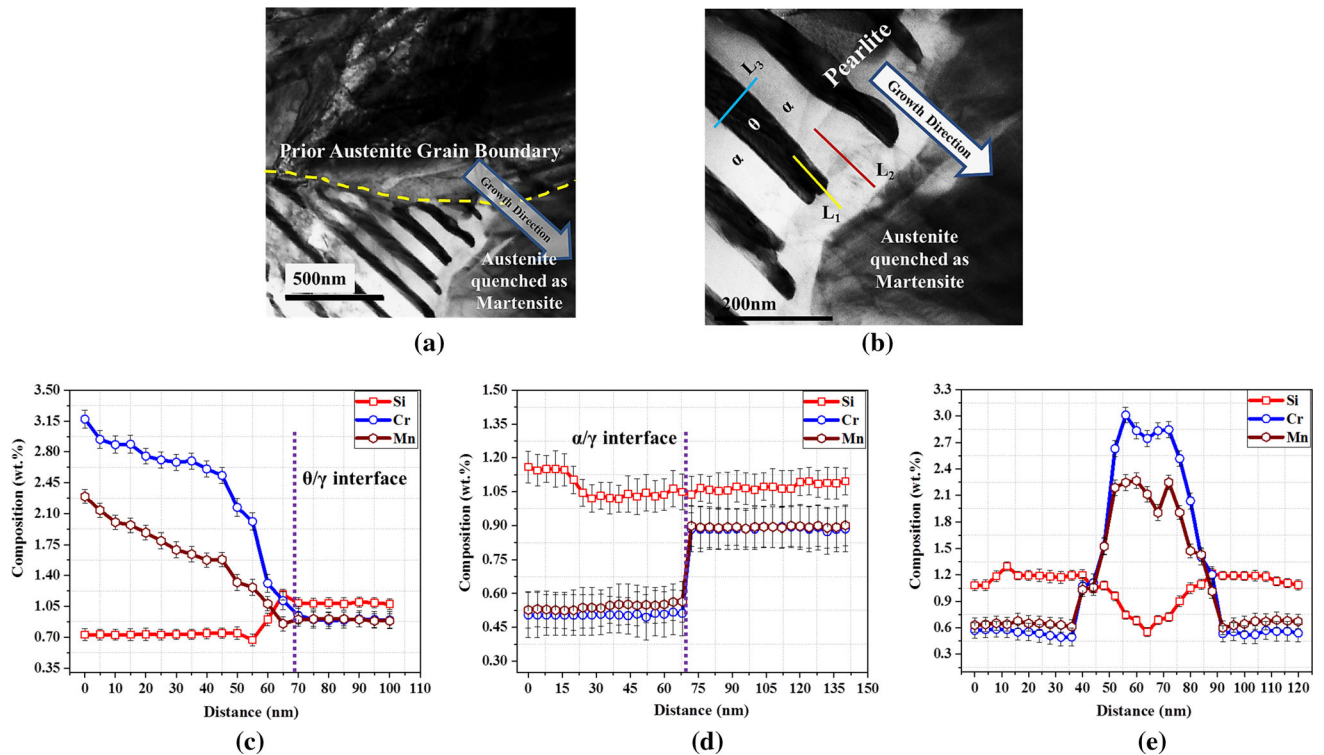


Fig. 4—A growing pearlite nodule in the S2 specimen for which (a) low magnification STEM BF micrograph with the highlighted growth direction and outlined prior austenite grain boundary from which it emanated, (b) high magnification STEM BF micrograph depicting the austenite/pearlite interface and the acquired multi-point EDS arrays along  $L_1$ ,  $L_2$  and  $L_3$ ; composition profile along (c)  $L_1$  across  $\theta/\gamma$  interface, (d)  $L_2$  across  $\alpha/\gamma$  interface and (e)  $L_3$  across  $\alpha/\theta/\alpha$  interface.

which is not possible for a fixed volume element of austenite transforming to pearlite. The expected ratio should be close to 8 (taking into account alloying element effect on carbon equivalent). This high apparent thickness of cementite lamella is indicative of the inclined character of the nodule in Figure 4(b). Therefore, it is to be noted here that the apparent interlamellar spacing observed in Figure 4(b) is not related to the pre-quench temperature, rather is a manifestation of intersection of pearlite nodules at shallow angles to the sample surface.

Similar to Figure 3(b) in Section III-B-1,  $L_1$ ,  $L_2$  and  $L_3$  in Figure 4(b) depict the linear arrays across  $\theta/\gamma$ ,  $\alpha/\gamma$ ,  $\alpha/\theta/\alpha$  interfaces, respectively, along which EDS was acquired. Lines  $L_1$ ,  $L_2$  and  $L_3$  in Figure 4(b) consist of 21, 36 and 31 points with 5, 4 and 4 nm separation between the points, respectively. It can be observed from the concentration profiles in Figure 4(c) that due to post transformation effects, the partitioning extent for Cr and Mn behind the interface increases with distance from the growth front. The local compositional change for Cr and Mn across  $\theta/\gamma$  interface also hints at possible partitioning led growth of pearlite nodule at  $\sim 660^\circ\text{C}$  (approx. temperature from which S2 was quenched). Complementary to the observations of Figure 4(c), a sharp change in the local composition of Cr and Mn across  $\alpha/\gamma$  interface (as observed in Figure 4(d)) provides confirmatory evidence of partitioning led local equilibrium during  $\alpha/\gamma$  growth at this instant of cooling. The relatively constant (or marginally depleting) level of Cr and Mn in ferrite with increasing distance behind the  $\alpha/\gamma$  growth front (Figure 4(d)) hints at minimal reach of post transformation partitioning effect to the center of the ferrite lamellae. The observation of partitioning mode of pearlite growth for Mn and Cr is in line with the past observations of Ridley *et al.* in Cr-Mn eutectoid steels when treated isothermally at temperatures close to  $660^\circ\text{C}$ .<sup>[17]</sup>

In case of Si, the relatively constant nature of the composition profile along with a sharp change across the  $\theta/\gamma$  interface (Figure 4(c)) clearly indicates interfacial diffusion-assisted partitioning led growth mode. Moreover the expected post transformation partitioning led depletion of Si from the center of cementite with increasing distance from growth front is observed to be minimal in Figure 4(c). This constancy can be attributed to the low diffusivity of Si in cementite. However, in contrast to the observation of Figure 4(c), the composition profile of Si across the center of  $\alpha/\gamma$  interface is constant as shown in Figure 4(d). This observation hints at the possibility of enrichment of ferrite being limited to the regions near the cementite lamella only (at the vicinity of  $\alpha/\gamma$  interface) during the interfacial partitioning process. The composition profile for Si acquired along  $L_3$  (at a distance of  $\sim 215$  nm from the growth front) as shown in Figure 4(e), also depicts that the ferritic regions adjacent to the cementite lamella possess marginally higher content than the center of ferrite even after post transformation partitioning. This observation supports the aforementioned possibility of interfacial partitioning led enrichment of ferrite being limited to regions near the cementite

lamella. Due to this reason the content of Si at the center of ferrite remains unaltered and hence close to the nominal composition, thereby leading to the observation of almost constant level across the  $\alpha/\gamma$  interface as observed in Figure 4(d). This observation of partitioning mode of pearlite growth for Si at  $660^\circ\text{C}$  is also in line with the past research works of Ridley *et al.* on Fe-Si-C systems.<sup>[18]</sup>

The slight increase in Si content within the center of ferrite far from the growth front (at  $\sim 20$  nm from left in Figure 4(d)) is the effect of post transformation partitioning. This sudden change in Si content within the center of ferrite at  $\sim 45$  nm from the growth front (Figure 4(d)) also hints at the possible spatial transition from no-partitioning to partitioning led growth mode. The same is also vaguely reflected by the composition profile of Mn within the center of ferrite which tends to increase marginally (from behind a distance of  $\sim 45$  nm) towards the growth front (Figure 4(d)).

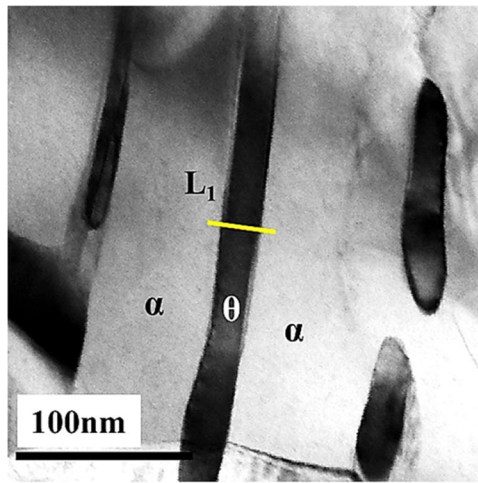
The composition profiles of Cr and Mn as shown in Figure 4(e) clearly indicate that the post transformation partitioning from ferrite to  $\alpha/\theta$  interface is faster as compared to that from  $\alpha/\theta$  interface to the center of cementite. This leads to the observed interfacial segregation of both the elements. From the composition profiles of Figure 4(e), it can be deduced that the rate of post transformation partitioning of Cr into cementite from ferrite is faster than that of Mn and the vice-versa of Si in the S2 specimen.

Similar to the case of S1, here also the minor deviations from smooth profile at some localized regions (*e.g.*, at  $\sim 12$  nm along  $L_3$  for the profile of Si,) can be attributed to local heterogeneity in sample thickness.

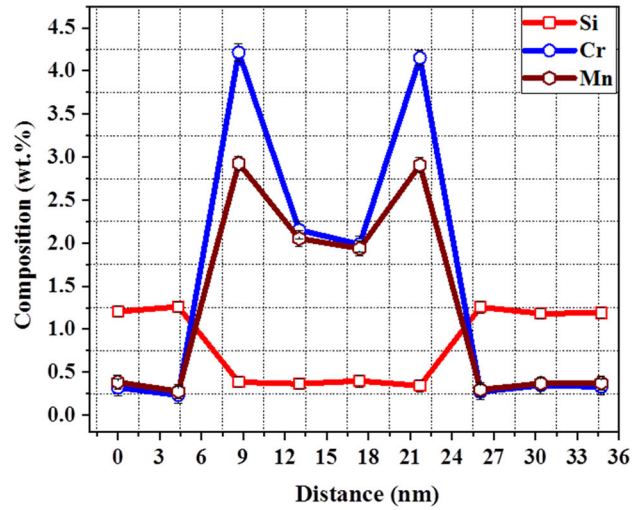
### 3. Partitioning studies in samples interrupted at $635^\circ\text{C}$ (S3)

The STEM BF micrograph of Figure 5(a) depicts ferrite/cementite lamellae in the S3 specimen. Figure 5(b) presents the multi-point EDS profile for Mn, Cr and Si as acquired along  $L_1$  across  $\alpha/\theta/\alpha$  interface shown in Figure 5(a). The linear array  $L_1$  consists of 9 points with 4 nm separation between each point. The observed width of cementite lamellae and the interlamellar spacing in Figure 5(a) do not represent the true values, rather are merely the projected dimensions, as a perfect alignment of  $\alpha/\theta/\alpha$  interface with the electron beam could not be attained. Therefore, similar to the case of S2, it is to be noted here that the apparent interlamellar spacing observed in Figure 5(a) is not related to the pre-quench temperature, rather is due to the pearlite nodule not being perpendicular to the sample surface. The  $\alpha/\theta$  interfacial segregation of Cr and Mn as shown in Figure 5(b) clearly indicates that the rate of post transformation partitioning from ferrite to  $\alpha/\theta$  interface is faster as compared to that from  $\alpha/\theta$  interface to the center of cementite. It can be inferred from Figure 5(b) that the post transformation partitioning of Cr to cementite is much faster than Mn as well as that of Si from cementite to ferrite.

The reason behind observed difference in the nature of  $\alpha/\theta/\alpha$ -Mn/Cr composition profile of S1 as compared to those of S2 and S3 is basically a synergistic effect of



(a)



(b)

Fig. 5—(a) STEM BF micrograph depicting ferrite/cementite lamellae of pearlite in S3 specimen with  $L_1$  across which multi-point EDS has been acquired; (b) composition profile acquired along  $L_1$  across the  $\alpha/\theta/\alpha$  interface.

adjacent area X-ray contribution and shallow composition profiles in cementite of S1 sample. The post transformation partitioning led composition profiles are expected to comprise of an interfacial enrichment/depletion on either side of the interface, the extent of which depends upon the duration of partitioning. This is usually followed by a drop/rise to the bulk composition level of the respective phase towards the center. In case of S1 (*i.e.*, Figure 3(e)), the duration of partitioning experienced by ferrite and cementite is lesser than S2 which in turn is lesser than S3. This leads to lesser enrichment (of Mn and Cr) on the cementite side of the interface for S1 as compared to S2 and S3 followed by a shallow drop to the nominal content within cementite. The increase in the composition dip within cementite from S2 to S3 evidently supports this phenomenon (Figure 4(e) and 5(b)). Such kind of an ‘interfacial enrichment followed by a shallow drop to nominal composition’ profile existing within cementite, when probed along a closely spaced linear array of points, is associated with overlap of interaction volumes of adjacent areas, thereby leading to a profile as shown in Figure 3(e). Similar arguments can be extended to Si wherein a more or less constant composition profile is observed in cementite of S1 as compared to centrally leaner profile in case of S2 (Figure 4(e)).

#### 4. Partitioning studies in samples interrupted at 350 °C (S4)

The sample quenched from 350 °C was expected to have undergone post transformation partitioning to a significant extent approaching the ortho-equilibrium contents at that temperature. Long range partitioning of substitutional elements at temperatures as low as ~ 350 °C can be safely assumed to be minimal due to very low atomic mobilities. Therefore, any reminiscent partitioning was anticipated to be present in the form of thin interfacial enrichment, for capturing which APT was done. Elemental atom maps obtained from APT

analysis (Figure 6(a)) depict the persistent  $\alpha/\theta$  interfacial enrichment of Cr at 350 °C (encircled region). The proxigrams depicting the composition profiles for all the elements across  $\alpha/\theta$  interface have been shown in Figure 6(b). The ortho-equilibrium  $\alpha/\theta$  and  $\theta/\alpha$  compositions for different elements as obtained from ThermoCalc<sup>®</sup> have been superimposed as dotted lines on the proxigrams in Figure 6(b). The ortho-equilibrium compositions of different elements are given in the same colour as their corresponding proxigrams. These composition profiles clearly show that all the alloying elements have attained the ortho-equilibrium distribution across ferrite and cementite lamella except for Cr. This reminiscent  $\alpha/\theta$  interfacial enrichment of Cr hints at its sluggish partitioning towards the later stages of cooling.

#### C. Competitive Character of Post Transformation Partitioning

The observations of elemental distribution across  $\alpha/\theta/\alpha$  interface in S1, S2, S3 and S4 clearly indicate the competitive character of post transformation substitutional partitioning. However, before proceeding on to the assessment of this competitive character, it is essential to ascertain that the initial state of the regions of interest (where  $\alpha/\theta/\alpha$  linescans were acquired) in the respective samples was identical. Precisely, it is essential to assert that the  $\alpha/\theta/\alpha$  interfacial regions considered for post transformation partitioning kinetics had formed under no-partitioning condition in S1, S2, S3 and S4. This will consequently also confirm the absence of any contribution from interfacial partitioning (*via* growth front) in the observed partitioning across  $\alpha/\theta/\alpha$  interfaces (Figure 3(e), 4(e), 5(b)).

As has been discussed in Section III-B-1 (Figure 3(c) and (d)), pearlitic transformation in S1 specimen occurred under no/negligible partitioning condition. This confirms the onset of post transformation



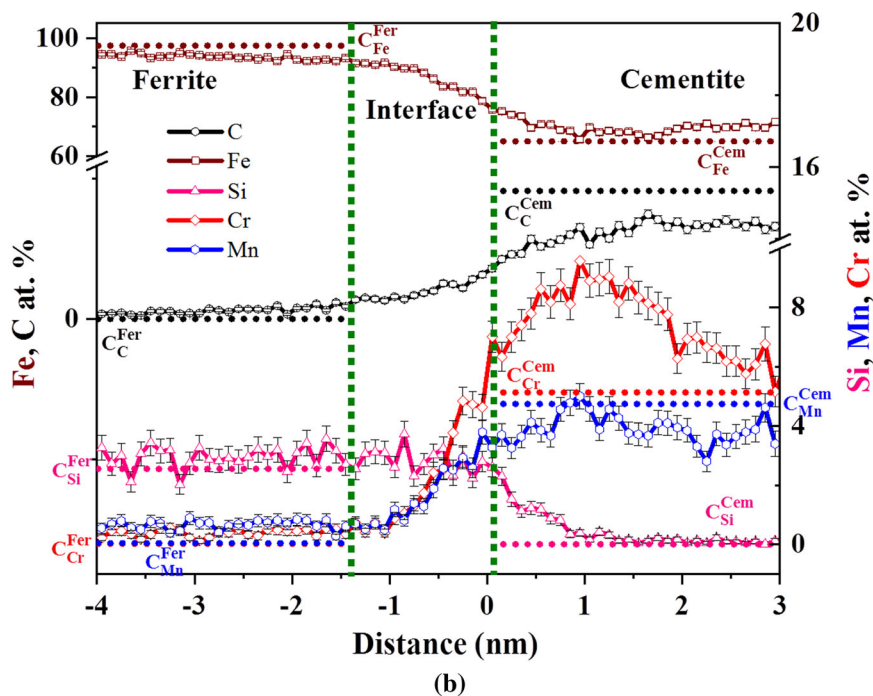
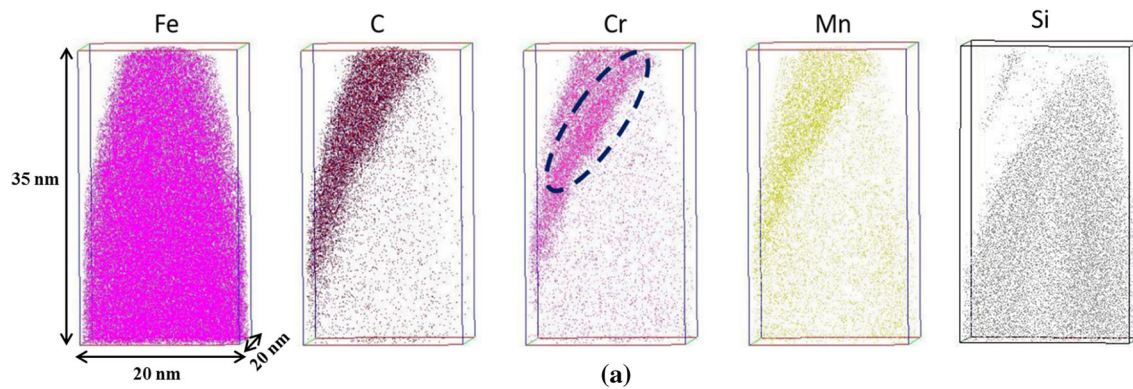


Fig. 6—(a) Elemental atom maps of a region containing a ferrite and cementite lamella, obtained by APT analysis on S4; (b) elemental distribution profile across  $\alpha/\theta$  interface obtained by proximity histogram technique, the dotted lines represent the  $\alpha/\theta$  and  $\theta/\alpha$  ortho-equilibrium compositions at 350 °C for different elements.

partitioning across  $\alpha/\theta$  interfaces from an initial state of nominal substitutional content (as that of the alloy under study) on both sides of the interface. It is also important to note here that, once the transformation proceeds under no-partitioning condition, with further decrease in transformation temperature (as in the present case of continuous cooling), the system would tend to continue under the same mode of transformation. This is because with decreasing temperature, the level of supersaturation with respect to product ( $\alpha$  and  $\theta$ ) formation increases along with simultaneously diminishing possibility of substitutional diffusion controlled mode.<sup>[3,5]</sup> Therefore, generally it is observed that transformation shifts from partitioning to no-partitioning mode as the temperature of transformation decreases.<sup>[3,16–19]</sup> Any observation of shift from no-partitioning mode to partitioning mode can be ascribed to the effect of soft impingement on reducing the growth

front velocity while pearlite transformation nears completion.

In case of S2, although the observed mode of pearlite formation at the growth front is led by partitioning of substitutional elements, yet the  $\alpha/\theta/\alpha$  interfacial region considered for post transformation partitioning kinetics can be assertively proven to have formed under no/negligible partitioning of substitutional elements. As already mentioned in Section III-B-2, the possible spatial transition from no-partitioning to partitioning mode of transformation is marked by the slight enhancement in the Si content within the center of ferrite at a distance of  $\sim 45$  nm from the growth front (Figure 4(d)). To prove that this position of  $\sim 45$  nm behind the growth front is actually the transition between no-partitioning to partitioning mode, the difference in growth front velocity at the transition point has to be determined. This in turn can be determined if

the velocity of growth front at 660 °C (*i.e.*, velocity at the tip of austenite pearlite interface of Figure 4(b)) can be estimated. For partitioning to be possible at the tip of growth front at 660 °C (as observed in Figure 4(c) and (d)), it is essential that the distance covered by growth front be less than the partitioning distance of components.<sup>[17]</sup> This is similar to the treatment given by Ridley *et al.* for Cr-Mn and Si containing eutectoid steels.<sup>[17,18]</sup> The distance to be covered by the components during partitioning is approximately half of the true interlamellar spacing (which is ~ 85 nm in the present case as observed from S1 and S3). Thus, the distance to be travelled by the components becomes ~ 42.25 nm. Since partitioning mode is clearly observable for Cr and Mn in S2, the assessment for growth front velocity is done by considering only these two substitutional components. The time (*t*) taken for partitioning of Cr and Mn over a distance of 'x' is given according to random walk theory as ' $x^2/2D_B$ ', where  $D_B$  corresponds to the boundary diffusion coefficient. The use of boundary diffusion coefficient instead of volume diffusion coefficient signifies that the growth front provides a short circuit diffusion path for substitutional partitioning.  $D_B$  can safely be assumed to be related to volume diffusion coefficient in ferrite ( $D_V$ ) by a factor of  $10^5$ , for dynamic boundaries such as the growth front in the present case.<sup>[17]</sup> The volume diffusion coefficient values for Cr and Mn in ferrite at 660 °C have been obtained from ThermoCalc<sup>®</sup> with TCFE9 + MOBFE4 database package as  $1.05 \times 10^{-20}$  m<sup>2</sup>/s and  $1.28 \times 10^{-19}$  m<sup>2</sup>/s, respectively. The corresponding boundary diffusivities when substituted into the equations of random walk theory lead to time, *t* equal to ~ 0.85 and 0.07 seconds for partitioning of Cr and Mn, respectively. Since Cr is found to take more time than Mn for partitioning, the rate controlling step for growth front movement can safely be assumed to be Cr partitioning. Further assuming the pearlite/austenite interface width to be ~ 3 nm (as estimated by Ridley *et al.* for Cr-Mn eutectoid steel<sup>[17]</sup>) at 660 °C, the time taken by the growth front to sweep this distance should be greater than 0.85 seconds so as to allow the partitioning of Cr (and Mn as well). This leads to a prediction of growth front velocity lesser than 3.5 nm/s which can favour interfacially assisted partitioning led growth of pearlite. It is, therefore, inferred from the aforementioned estimation that, the interface velocity that can sustain partitioning mode of pearlite growth at temperatures close to 660 °C is ~ 3.5 nm/s for the present alloy. Furthermore, from Figure 2(b), it can be clearly seen that the growth front velocity at ~ 663 °C is ~ 100 nm/s. With such a high growth front velocity in conjunction with not so different boundary diffusivity values (as compared to those at 660 °C), the partitioning of Cr and Mn would require an interface width of ~ 85 nm (following the similar procedure as above) which is highly unrealistic. Therefore, it can also be inferred that within 663 °C to 660 °C there is a drop in growth front velocity from 100 nm/s to ~ 3.5 nm/s, probably owing to soft impingement as pearlite transformation nears completion. The drop in temperature from 663 °C to 660 °C is

attained within a timespan of ~ 10 seconds, as the cooling rate during this stage of slow cooling was recorded to be ~ 0.3 °C/s (Figure 2(a)). Within this timespan, the growth front would have traversed ~ 35 nm, considering the estimated interface velocity of 3.5 nm/s for partitioning mode of pearlite formation at 660 °C. This is close to the distance (~45 nm) from the growth front which was considered as the spatial transition from no-partitioning to partitioning mode of transformation as mentioned in Section III-B-2. The acquired  $\alpha/\theta/\alpha$  linescan in S2 is at a distance of ~ 215 nm from the growth front which is clearly very far from the no-partitioning to partitioning transition zone and therefore can safely be assumed to have formed under no-partitioning condition.

In case of S3, the composition measurements at various points along the length of cementite lamella (Figure 5(a)) revealed the decreasing Cr and Mn content towards the top (away from the boundary at bottom). This confirmed the point of origin of the pearlite colony (bottom boundary) and hence the assumption that the region of  $\alpha/\theta/\alpha$  interface considered for post transformation partitioning kinetics assessment would have formed quite early under no/negligible partitioning condition.

These assessments confirm that majority of pearlitic transformation took place under no-partitioning condition and only towards the completion of transformation (at around 660 °C) there is a shift to partitioning led growth mode (perhaps owing to soft impingement). Therefore, it is expected that the  $\alpha/\theta$  lamellae of S4 sample (quenched at 350 °C) considered for APT analysis would have also transformed under no-partitioning condition.

Once the initial states of  $\alpha/\theta/\alpha$  regions of all the four samples have been ascertained to be identical, the post transformation partitioning kinetics can be subjected to evaluation for determination of the competitive character of the different components. However, it is to be noted here that to clearly demarcate the competitiveness amongst the substitutional elements for post transformation partitioning, contents at the  $\alpha/\theta$  interface must be considered rather than that at the center of  $\alpha$  or  $\theta$ . This is because the content at the center is dictated primarily by the abundance of individual element available for exchange whereas the content at the interface is primarily a reflection of the chemical potential gradient led partitioning. Figure 7 makes this notion evidently clear wherein the composition of the substitutional elements at the center of the cementite lamellae and at the cementite side of the  $\alpha/\theta$  interface are shown in (a) and (b) respectively.

The substitutional contents in Figure 7 have been deduced from the STEM-EDS compositions acquired on S1, S2 and S3, considering only the substitutional sub-lattice. The composition acquired on S4 has not been used in this analysis as it had almost approached equilibrium content for all the substitutional elements in respective phases. As can be seen from Figure 7(a), the variation of substitutional content, especially Fe at the center of cementite lamellae is not systematic with

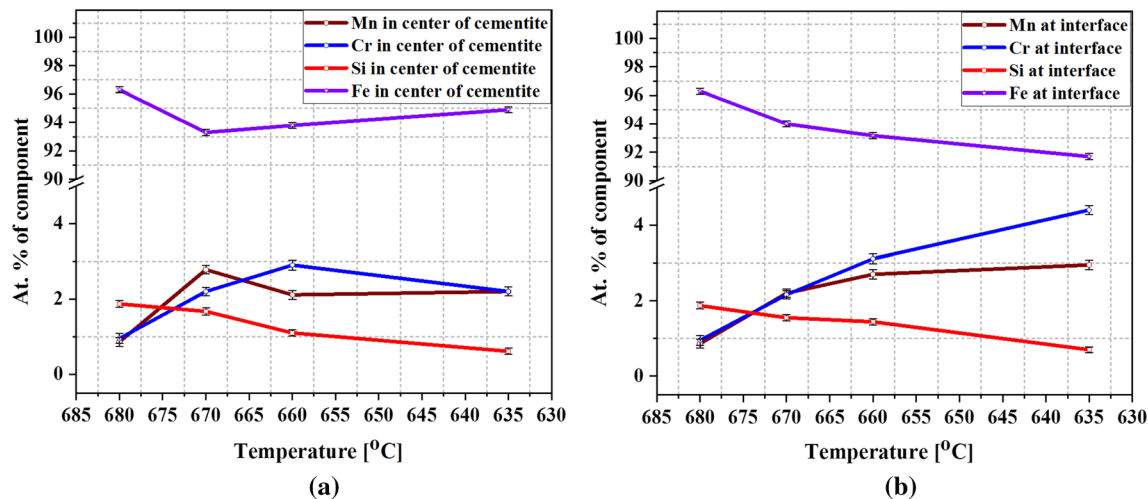


Fig. 7—Variation of substitutional content with temperature during cooling (a) at the center of cementite lamellae and (b) at the cementite side of the  $\alpha/\theta$  interface.

respect to temperature. This is probably because of the higher tendency for exchange with Si (cementite destabilizer) owing to its greater abundance. On the other hand, the variation of substitutional content at the cementite side of the  $\alpha/\theta$  interface clearly presents the competitive behaviour with respect to temperature during cooling.

To further understand the underlying mechanism of this competitive character of post transformation partitioning, a simulation was setup in DICTRA<sup>®</sup> keeping the width of ferrite and cementite domain as 72 nm (with 144 grids) and 12.5 nm (with 25 grids), respectively. The initial concentration of substitutional elements was kept constant throughout ferrite and cementite (*i.e.*, non-partitioned pearlite) and the experimentally obtained 2<sup>nd</sup> stage cooling profile was applied.

Figure 8(a) shows the variation in diffusivity of different elements in ferrite and cementite with respect to temperature. The evolution of cementite side of  $\alpha/\theta$  interface composition with respect to partitioning time is shown in Figure 8(b) wherein it is clear that the rate of partitioning of Mn is higher than that of Cr within 0.1 seconds of the onset of simulation. This is due to the higher tendency of Mn to exchange with the Fe atoms which diffuse out of cementite rapidly as soon as partitioning commences (Figure 8(c)). This explains the experimental observation of higher rate of Mn partitioning in the S1 specimen at a distance of ~175 nm from the growth front ( $L_3$  in Figure 3(b)), which would have experienced an effective partitioning time of ~0.1-0.2 seconds, assuming front velocity close to the measured values by MNR method at 670 °C (Figure 2(b)). The higher rate of Cr partitioning during the intermediate stages as observed in Figure 4(e) and 5(b), can be explained with the help of Figure 8(c) wherein the higher Cr content at the cementite side of interface till ~200 seconds indicates its greater cementite stabilizing capability than Mn and Fe. After ~260 seconds of cooling, Mn partitioning to cementite would be accelerated due to its greater cementite stabilizing capability than that of Cr (Figure 8(c)). This is what

leads to the completion of Mn partitioning earlier than Cr as observed in Figure 6(b). The reminiscent pile up of Cr (as observed in Figure 6(b)) would dissipate with time and the entire thickness of cementite lamella would attain the ortho-equilibrium composition. It can be easily assessed from Figure 6(b) that the enrichment extends over a distance of ~3 nm towards the cementite side of interface, which after dissipation would level up at ~5 at.pct *i.e.*, close to the ortho-equilibrium prediction within half of the thickness of cementite (assuming axi-symmetric condition). Similar results of reminiscent interfacial enrichment owing to differential diffusivity in ferrite and cementite have been reported by Miller *et al.* for Mn in pearlitic steels.<sup>[50]</sup> On the other hand, Si despite of having the lowest diffusivity in cementite has reached ortho-equilibrium level in ferrite because of relatively shorter distance to be covered within cementite during post transformation partitioning (*i.e.*, half of cementite width). The diffusivity of Si in ferrite is, however, comparable to (in fact higher) Cr, leading to quicker dissipation and achievement of ortho-equilibrium levels (Figure 6(b)).

The experimental variation of substitutional content with respect to temperature during 2<sup>nd</sup> stage cooling (or equivalently the time instance during cooling) as presented in Figure 7(b) qualitatively conforms to theoretical trend as shown in Figure 8(c).

To assess the quantitative proximity of experimental observation and theoretical simulation, the composition at the cementite side of the interface after 135 seconds of simulation time was compared with that acquired by STEM EDS of S3.

Figures 9(a)-(c) show the simulated composition profiles for Cr, Si and Mn after 135 seconds of simulation time wherein substitutional spikes within a narrow zone of ~0.5 nm exist at the interface. To compare these simulation results with EDS data, each composition profile has been discretely averaged over 2 nm distance about the interface on both ferrite and cementite sides and superimposed over respective profiles. These discretely averaged compositions are given

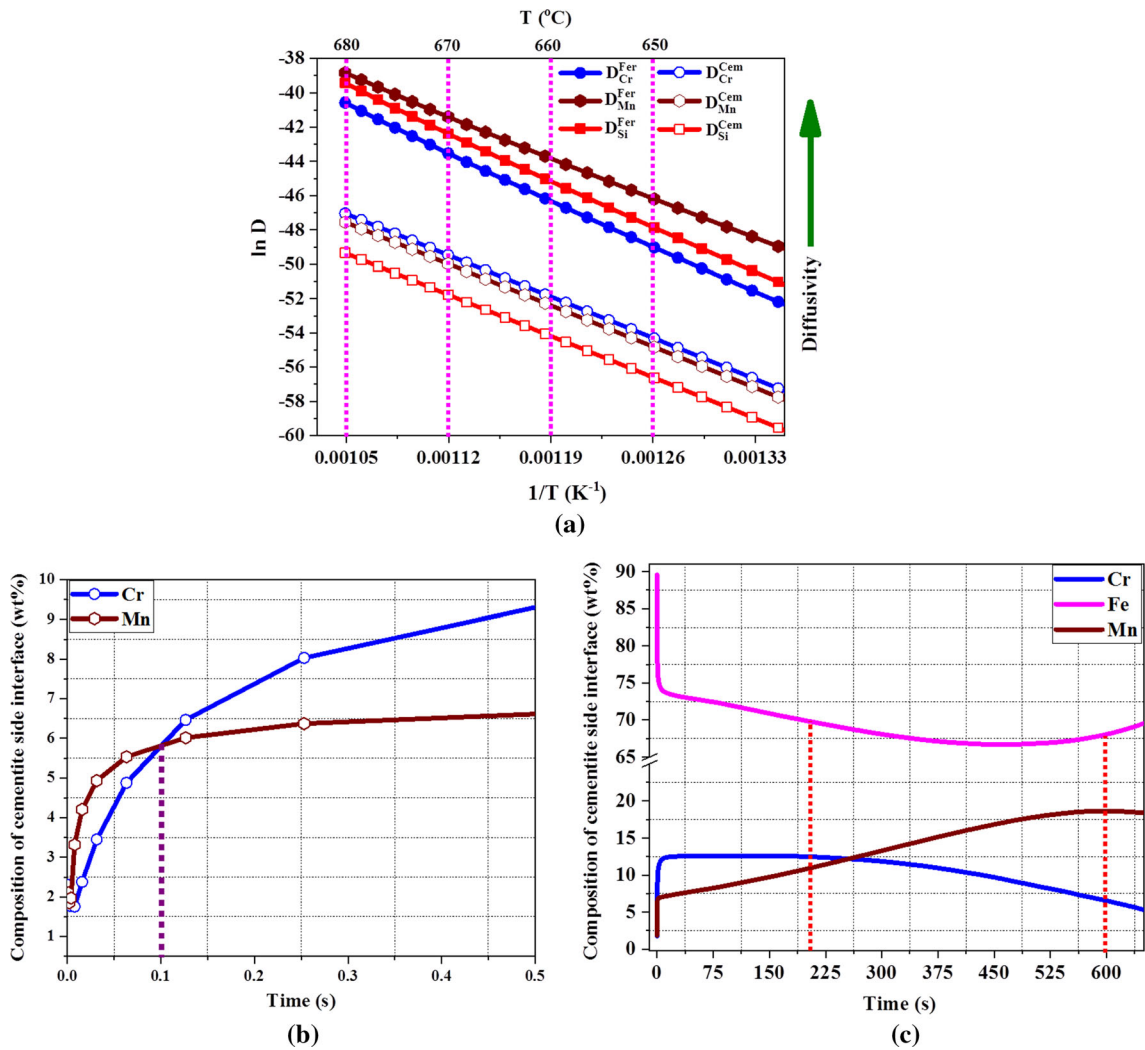
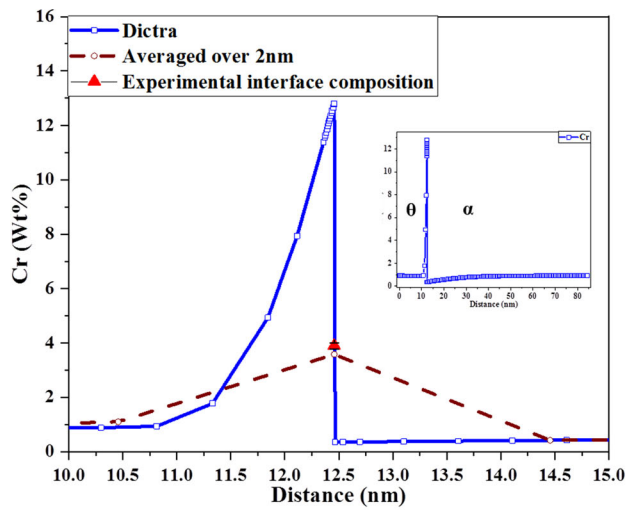


Fig. 8—(a) Variation in diffusivity of Cr, Mn and Si for both  $\alpha$  and  $\theta$  phases with respect to temperature- $\ln D$  vs  $1/T$  plot; variation in the equilibrium composition of cementite side of the  $\alpha/\theta$  interface with respect to partitioning time till: (b) 0.5 seconds and (c) 650 seconds, here the vertical dotted lines depict the time interval within which the Mn enrichment stabilizes cementite by replacing Fe.

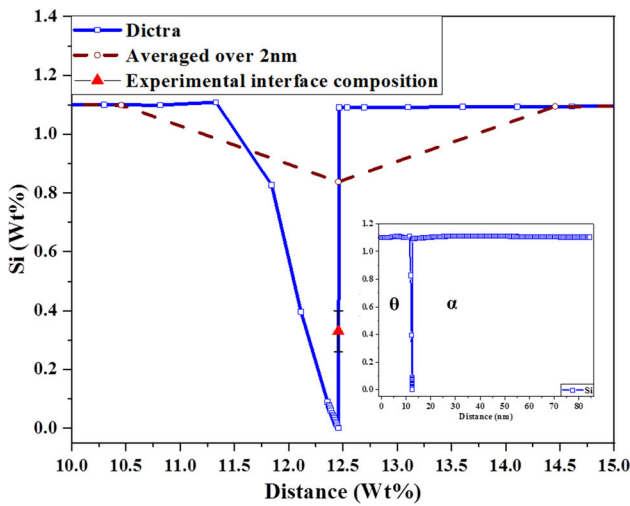
as dashed profiles in Figure 9(a)-(c). The EDS results of S3 specimen were used for comparison, because the duration for which the ferrite/cementite lamellae here would have experienced partitioning is expected to be  $\sim 135$  seconds due to an observed incubation period of  $\sim 14$  seconds prior to pearlite formation. The comparison of the substitutional contents at the cementite side of the interface has been done by considering the total composition (including interstitial content) rather than the substitutional sublattice only.

The EDS compositions at the cementite side of interface (given by red triangles) are found to lie close to the simulation results (Figures 9(a)-(c)). The differences between the two in case of Cr and Mn ((a) and (c)) can be attributed to the actual time for which  $L_1$  in Figure 5(a) would have experienced sidewise partitioning. In case of Si, however, DICTRA<sup>®</sup> underestimates the extent of partitioning which can be attributed to growth front led diffusion at the later stages of transformation when the front velocity is very low.<sup>[11]</sup> It is worthwhile to note here that the compositions presented

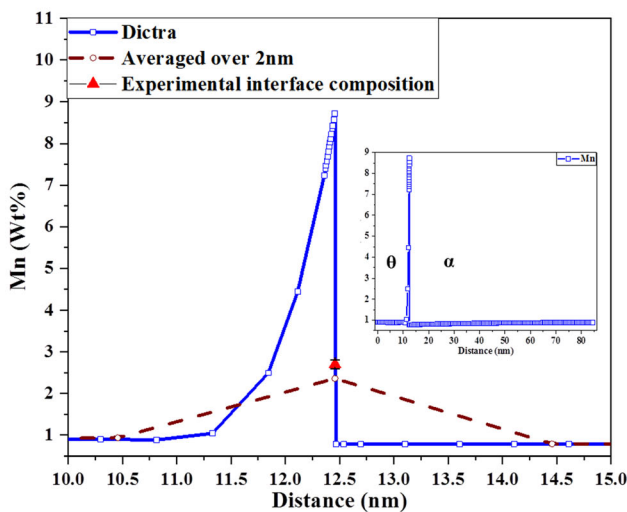
in Figure 8(b), (c) and Figure 9(a)-(c) are different than those denoted by dotted lines in Figure 6(b). This is because in Figure 6(b), the ortho-equilibrium (*i.e.*, when the respective phases are in completely stable conditions) compositions of ferrite and cementite at 350 °C have been presented, while Figures 8 and 9 present the metastable equilibrium compositions achieved by cementite during post transformation partitioning simulation. These metastable compositions of cementite evolve with respect to temperature (as simulated by DICTRA<sup>®</sup>), when the diffusion setup consisting of ferrite and cementite starts with nominal alloy composition across the common interface. It is thermodynamically expected that since initially cementite is forced to contain excess Si during the DICTRA<sup>®</sup> simulation, it becomes metastable and under metastable conditions, the solubility of Mn and Cr (or any other stabilizing solute) would be higher as compared to that prevailing under stable ortho-equilibrium conditions. In other words, the compositions presented in Figure 8 and 9 are basically the transient metastable equilibrium



(a)



(b)



(c)

◀ Fig. 9—DICTRA<sup>®</sup> simulated composition profiles about ferrite/cementite interface using TCFE9<sup>®</sup> + MOBFE4<sup>®</sup> databases after 135 seconds of simulation period for: (a) Cr, (b) Si and (c) Mn wherein the composition profiles for the respective components over the entire domain of simulation are given as insets. Composition profiles calculated by discretely averaging each simulation profile over 2 nm distance are also shown as brown dashed lines in the respective figures for Cr, Si and Mn. The experimentally observed composition of cementite side interface in the S3 specimen for Cr, Si and Mn are also superimposed as red solid triangles in (a)-(c), respectively (Color figure online).

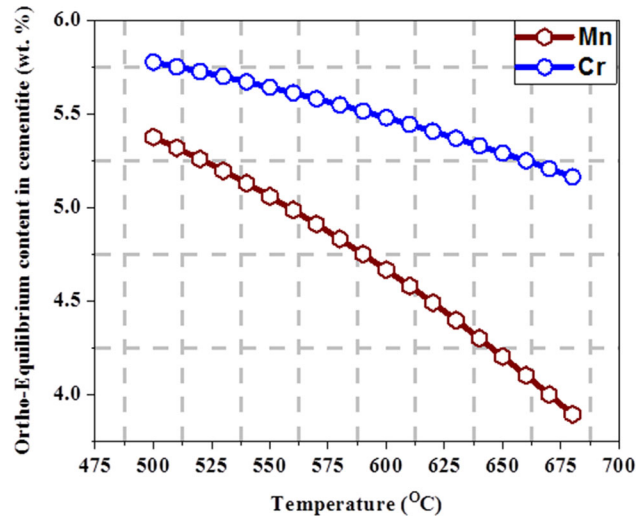


Fig. 10—Variation of ortho-equilibrium Mn and Cr content in cementite with respect to temperature-property diagram computed using ThermoCalc<sup>®</sup>.

compositions of cementite while it approaches the most stable ortho-equilibrium state and that is why they differ from the compositions presented in Figure 6(b). Within these transient metastable equilibria compositions, there are cross-overs between Mn and Cr as seen in Figures 8, representing the relative cementite stabilizing effect of the respective components with respect to temperature.

As already mentioned, the observed sluggish partitioning and reminiscent interfacial enrichment of Cr as compared to Mn and Si towards the completion of partitioning (Figure 6(a) and (b)), can be attributed to the decreasing diffusivity of Cr in ferrite (as compared to Mn and Si in Figure 8(a)) along with its decreasing cementite stabilizing effect, as depicted by the equilibrium  $\theta/\alpha$  composition (refer Figure 8(c)). The decreasing cementite stabilizing effect of Cr as compared to that of Mn is clear from Figure 10 which depicts the ortho-equilibrium content of Mn and Cr in cementite with respect to temperature. It can evidently be seen from the slope of curves in Figure 10 that the cementite stabilizing effect of Cr is higher at high temperatures whereas Mn supersedes Cr in stabilizing cementite at lower temperatures.

**Table II. Partitioning Behaviour at Different Stages During Nano-Pearlitic Transformation**

Sample	Temperature from which sample was quenched for partitioning studies	Observation
S1	~ 670 °C	no partitioning across the growth front
S2	~ 660 °C	post transformation partitioning of Mn is fastest
S3	~ 635 °C	partitioning across the growth front post Transformation partitioning of Cr is fastest
S4	~ 350 °C	pearlite transformation is complete post Transformation partitioning of Cr is fastest all the elements have attained ortho-equilibrium composition in respective phases except Cr. interfacial enrichment of Cr on the cementite side is still persistent indicating slowest partitioning kinetics towards completion

The observed partitioning behaviour, either during transformation or post transformation has been collated in Table II.

#### IV. CONCLUSION

Summarily, an attempt at understanding the elemental partitioning behaviour during nano-pearlitic transformation (interlamellar spacing < 100 nm) has been made in the present study. The alloy under study exhibits a non-partitioned pearlite growth for majority of the transformation duration which further undergoes post transformation partitioning. The assessment of elemental partitioning has been done by interrupting the designed two stage cooling process and performing STEM-EDS as well as APT. The experimental assessment shows that the post transformation partitioning rate of Mn is highest at the onset. This is followed by Cr being the fastest for a reasonable fraction of time as compared to Mn and Si. However, towards the end, Mn and Si partition faster than Cr leading to sustained interfacial enrichment at the ferrite/cementite interface. The plausible underlying mechanisms are deduced by theoretical simulation of post transformation partitioning using DICTRA<sup>®</sup>. The initially faster partitioning of Mn is because of its greater tendency to exchange with Fe (as compared to Cr and Si) which leaves cementite as soon as partitioning commences. The dominance of Cr partitioning for the intermediate time period is because of its greater cementite stabilizing capability as compared to Mn. Si although possesses greater chemical potential gradient was found to possess more or less constant partitioning rate, perhaps owing to its lower mobility. However, towards the completion, Mn and Si have much faster partitioning rate as compared to Cr due to dominance of cementite stabilizing effect.

#### ACKNOWLEDGMENT

The authors would like to express their sincere thanks to Dr. M.M. Humane and Mr. R.K. Minj for their support throughout this work. The authors

would also like to thank The Director, CSIR- NML for providing the financial support (through i-PSG-0303 and MLP 3123) to carry out this work and his kind permission to publish it.

#### CONFLICT OF INTEREST

The authors declare that they have no conflict of interest.

#### REFERENCES

1. D. Embury: The formation of pearlite in steels, in *Phase Transformation in steels*, vol. 1, E. Pereloma and D.V. Edmonds, eds., Woodhead Publishing Limited, Cambridge, 2012, pp. 276–307.
2. M. Hillert: *Acta Metall.*, 1971, vol. 19, pp. 769–78.
3. R.C. Sharma, G.R. Purdy, and J.S. Kirkaldy: *Metall. Trans. A.*, 1979, vol. 10, pp. 1119–27.
4. R.C. Sharma, G.R. Purdy, and J.S. Kirkaldy: *Metall. Trans. A.*, 1979, vol. 10, pp. 1129–39.
5. S.K. Tewari and R.C. Sharma: *Metall. Trans. A.*, 1985, vol. 16, pp. 597–603.
6. J.W. Cahn and W.C. Hagel: Theory of pearlite reaction, in *The selected works of John W. W.C. Carter and W.C. Johnson*, eds., The Minerals, Metals and Materials Society, Cahn, 1998, pp. 133–98.
7. J.Y. Yan, J. Ågren, and J. Jeppsson: *Metall. Mater. Trans. A.*, 2020, vol. 51, pp. 1978–2001.
8. A. Borgenstam, D. Edmonds, and M. Hillert: *Acta Mater.*, 2016, vol. 103, pp. 280–89.
9. M.M. Aranda, R. Rementeria, C. Capdevila, and R.E. Hackenberg: *Metall. Mater. Trans. A.*, 2016, vol. 47, pp. 649–60.
10. Z.Q. Liu, G. Miyamoto, Z.G. Yang, and T. Furuhashi: *Metall. Mater. Trans. A.*, 2013, vol. 44, pp. 5456–67.
11. A.S. Pandit and H.K.D.H. Bhadeshia: *Proc. R. Soc. A*, 2011, vol. 467, pp. 2948–61.
12. M. Hillert and J. Ågren: *Scr. Mater.*, 2004, vol. 50, pp. 697–99.
13. M. Hillert, J. Odqvist, and J. Ågren: *Scr. Mater.*, 2004, vol. 50, pp. 547–50.
14. G. Purdy, J. Ågren, A. Borgenstam, Y. Bréchet, M. Enomoto, T. Furuhashi, E. Gamsjäger, M. Gouné, M. Hillert, C.R. Hutchinson, M. Militzer, and H. Zurob: *Metall. Mater. Trans. A.*, 2011, vol. 42, pp. 3703–18.
15. M. Gouné, F. Danoix, J. Ågren, Y. Bréchet, C.R. Hutchinson, M. Militzer, G. Purdy, S. van der Zwaag, and H. Zurob: *Mater. Sci. Eng. R.*, 2015, vol. 92, pp. 1–38.
16. N.A. Razik, G.W. Lorimer, and N. Ridley: *Metall. Trans. A.*, 1976, vol. 7, pp. 209–14.
17. S.A. Al-Salman, G.W. Lorimer, and N. Ridley: *Metall. Trans. A.*, 1979, vol. 10, pp. 1703–09.

18. S.A. Al-Salman, G.W. Lorimer, and N. Ridley: *Acta Metall.*, 1979, vol. 27, pp. 1391–1400.
19. J. Chance and N. Ridley: *Metall. Trans. A.*, 1981, vol. 12, pp. 1205–13.
20. N. Ridley: *Metall. Trans. A.*, 1984, vol. 15, pp. 1019–36.
21. N. Ridley, M.A. Malik, and G.W. Lorimer: *Mater. Charact.*, 1990, vol. 25, pp. 125–41.
22. C.R. Hutchinson, R.E. Hackenberg, and G.J. Shiflet: *Acta Mater.*, 2004, vol. 52, pp. 3565–85.
23. M.M. Aranda, R. Rementeria, J. Poplawsky, E. Urones-Garrote, and C. Capdevila: *Scr. Mater.*, 2015, vol. 104, pp. 67–70.
24. M.M. Aranda, R. Rementeria, R. Hackenberg, E. Urones-Garrote, S.P. Tsai, J.R. Yang, and C. Capdevila: *Materials.*, 2016, vol. 9, pp. 988–98.
25. H. Ishigami, N. Nakada, T. Kochi, and S. Nanba: *ISIJ Int.*, 2019, vol. 59, pp. 1667–75.
26. K.M. Wu and H.K.D.H Bhadeshia: *Scr. Mater.*, 2012, vol. 67, pp. 53–56.
27. M. Ueda, K. Uchino, K. Matsushita and A. Kobayashi, Nippon Steel Technical Report No. 85, 2002, pp. 167–172.
28. B.L. Bramfitt, F.B. Fletcher, J.A. Davis Jr., Patent US 8721807B2, 2014.
29. H.S. Zurob, C.R. Hutchinson, A. Beche, G.R. Purdy, and Y.J.M. Brechet: *Acta Mater.*, 2008, vol. 56, pp. 2203–11.
30. Z.Q. Liu, G. Miyamoto, Z.G. Yang, and T. Furuvara: *Acta Mater.*, 2013, vol. 61, pp. 3120–29.
31. M. Enomoto, N. Maruyama, K.M. Wu, and T. Tarui: *Mater. Sci. Eng. A.*, 2003, vol. 343, pp. 151–57.
32. H.P. Van Landeghem, B. Langelier, B. Gault, D. Panahi, A. Korinek, G.R. Purdy and H.S. Zurob, *Acta Mater.*, 2017, vol. 124, pp. 536–43.
33. G. Miyamoto, K. Yokoyama, and T. Furuvara: *Acta Mater.*, 2019, vol. 177, pp. 187–97.
34. E.D. Hondros: *Mater. Sci. Eng. A*, 1993, vol. 166, pp. 1–10.
35. J.B. Seol, J.W. Bae, Z. Li, J.C. Han, J.G. Kim, D. Raabe, and H.S. Kim: *Acta Mater.*, 2018, vol. 151, pp. 366–76.
36. T. Tarui, A. Yoshie, Y. Asano, T. Takahashi, S. Nishida, H. Ohba and I. Ochiai, Nippon Steel Technical Report No. 80, 1999, pp. 44–49.
37. C. Tian, H. Guo, B. Hu, M. Enomoto and C. Shang, *Mater. Sci. Eng. A*, 2021, vol. 810, 141009.
38. P.S.M. Jena, S. Tripathy, B. Mahato, and J.K. Sahu: *Phil. Mag. Lett.*, 2019, vol. 99, pp. 284–91.
39. J.B. Gilmour, G.R. Purdy, and J.S. Kirkaldy: *Metall. Trans.*, 1972, vol. 3, pp. 1455–64.
40. H. Guo and M. Enomoto: *Metall. Mater. Trans. A.*, 2007, vol. 38, pp. 1152–61.
41. A.D. Pelton and C.W. Bale: *Metall. Trans. A.*, 1986, vol. 17, pp. 1211–15.
42. C.W. Bale and A.D. Pelton: *Metall. Trans. A.*, 1990, vol. 21, pp. 1997–2002.
43. G. Ghosh and G.B. Olson: *Acta Mater.*, 2002, vol. 50, pp. 2099–19.
44. W. Sha, L. Chang, G.D.W. Smith, L. Cheng, and E.J. Mittemeijer: *Surf. Sci.*, 1992, vol. 266, pp. 416–23.
45. J. Takahashi, T. Tarui, and K. Kawakami: *Ultramicroscopy.*, 2009, vol. 109, pp. 193–99.
46. A. Biswas, D. Sen, S.K. Sarkar, Sarita, S. Mazumder and D.N. Seidman, *Acta Mater.*, 2016, vol. 116, pp. 219–30.
47. A. Durgaprasad, S. Giri, S. Lenka, S.K. Sarkar, A. Biswas, S. Kundu, S. Mishra, S. Chandra, R.D. Doherty, and I. Samajdar: *Metall. Mater. Trans. A.*, 2018, vol. 49, pp. 2037–47.
48. O.C. Hellman, J.A. Vandenbroucke, J. Rüsing, D. Isheim, and D.N. Seidman: *Microsc. Microanal.*, 2000, vol. 6, pp. 437–44.
49. J.W. Cahn and W.C. Hagel: *Acta Metall.*, 1963, vol. 11, pp. 561–74.
50. M.K. Miller, P.A. Beaven, R.J. Lewis, and G.D.W. Smith: *Surf. Sci.*, 1978, vol. 70, pp. 470–84.

**Publisher's Note** Springer Nature remains neutral with regard to jurisdictional claims in published maps and institutional affiliations.